Application of the body of revolution finite-element method in a re-entrant cavity for fast and accurate dielectric parameter measurements

Tianqi Feng(冯天琦), Chengyong Yu(余承勇)†, En Li(李恩), and Yu Shi(石玉)

School of Electronic Science and Engineering, University of Electronic Science and Technology of China, Chengdu 611731, *China*

(Received 18 February 2022; revised manuscript received 14 June 2022; accepted manuscript online 8 July 2022)

In dielectrometry, traditional analytical and numerical algorithms are difficultly employed in complex resonant cavities. For a special kind of structure (a rotating resonant cavity), the body of revolution finite-element method (BOR-FEM) is employed to calculate the resonant parameters and dielectric parameters. In this paper, several typical resonant structures are selected for analysis and verification. Compared with the resonance parameter values in the literature and the simulation results of commercial software, the error of the BOR-FEM calculation is less than 0.9% and a single solution time is less than 1 s. Reentrant coaxial resonant cavities loaded with dielectric materials are analyzed using this method and compared with simulation results, showing good agreement. Finally, in this paper, the established BOR-FEM method is successfully applied with a machined cavity for the accurate measurement of the complex dielectric constant of dielectric materials. The test specimens were machined from polytetrafluoroethylene, fused silica and Al_2O_3, and the test results showed good agreement with the literature reference values.

Keywords: microwave, resonance method, dielectric measurement, coaxial resonant cavity

PACS: 01.40.gf **DOI:** 10.1088/1674-1056/ac7f91

1. Introduction

Dielectric materials — insulating materials with good electrical storage capacity — are important materials applied in the manufacture of microwave printed circuit board substrates,[1] dielectric resonators, radomes, etc.[2,3] Therefore, accurate measurement of their dielectric parameters is a key procedure for accurate evaluation of the performance of these devices. The popular techniques for dielectric measurement include waveguide structures (transmission or/and reflection), free-space methods and resonance methods,[4–7] of which the resonance methods can provide high-precision complex permittivity measurements for low-loss dielectrics.[8–13]

Re-entrant resonant cavities are employed for the measurement of dielectric materials in the resonance method.[14–16] A re-entrant cavity, shown in Fig. 1, consists of a coaxial line with end walls and an air gap between the inner conductor and the outer conductor. This structure has a very high test sensitivity since the electric field at the gap is very concentrated, and it is easy to achieve broadband measurements.[17–19] In order to place samples easily and enhance the repeatability of measurements, Xi and Tinga[20] adopted re-entrant cavities, shown in Fig. 2, with insertion holes below the cutoff frequency; these eliminate the radiation of the electromagnetic field in the top hole and reduce the influence from the non-flat bottom of the hole. The slits have a little effect on TM modes while restraining TE modes. This setup was used in the present work.

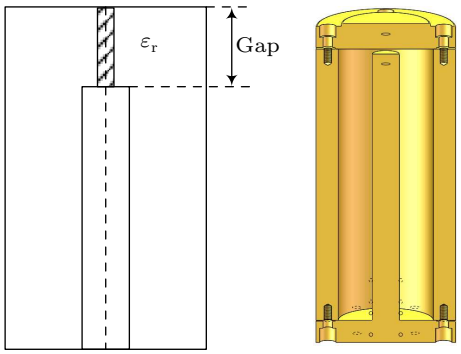


Fig. 1. A coaxial re-entrant cavity with a gap partially filled with a dielectric.

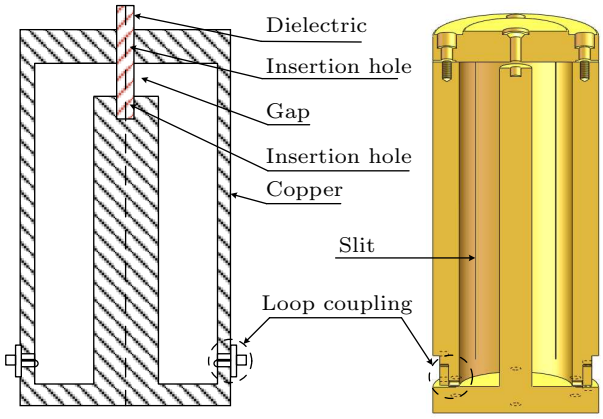


Fig. 2. A re-entrant cavity with an insertion hole.

In the measurement of material dielectric parameters there are two types of methods for theoretical electromagnetic analysis: analytical algorithms and numerical algorithms.

†Corresponding author. E-mail: yu_cyong@163.com

© 2023 Chinese Physical Society and IOP Publishing Ltd

Analytical algorithms, including the mode matching (MM) method,[21] transverse-resonance techniques[22] and full-wave circuit analysis methods,[23] can provide highly accurate solutions and require only a short computing time. However, only specific and relatively simple structures such as that in Fig. 1 can be solved easily by those algorithms, which suffer convergence problems in complex structures[24,25] such as a re-entrant cavity with an insertion hole as shown in Fig. 2. Compared with analytical algorithms, numerical algorithms, including the finite-difference time-domain (FDTD) method[23,26,27] and the finite-element method (FEM),[23,27–29] can theoretically solve for arbitrary regions. Measuring a dielectric requires high accuracy; however, it demands numerical algorithms to disperse too many meshes, leading to long computation times[14,23,24,30] that are impractical.

For a special type of structure, the body of revolution (BOR), symmetric about the rotation axis, allows problems to be computed efficiently by employing two-dimensional (2D) numerical algorithms,[31–34] significantly reducing the computational difficulty. Therefore, the main purpose of this paper is to measure the resonant frequencies and the dielectric parameters exactly and efficiently by using a FEM based on the BOR (BOR-FEM) and then demonstrate the computational accuracy and efficiency of this method according to simulations and experiments.

The rest of this article is organized as follows. Section 2 derives the FEM equation based on BOR characteristics. In order to improve the computational performance between resonance and dielectric parameters, the forward/inversion derivation of generalized eigenvalue problems is described in Section 3. The forward method is proposed to solve the non-standard generalized eigenvalue problem in the case of computing resonant parameters with known dielectric parameters. The inversion method is applied to avoid the tedious work required to determine dielectric parameters that continuously sets the dielectric parameters to match the computed resonant parameters to the measured ones[2,3,35] when extracting dielectric parameters with measured resonant parameters. In Section 4, to demonstrate the high accuracy and efficiency of the proposed method (BOR-FEM), literature and Ansoft High Frequency Structure Simulator (HFSS) values are compared. In Section 5, the dielectric samples [polytetrafluoroethylene (PTFE), fused silica, and Al_2O_3] were measured by the proposed method and compared with measured values in the literature. Comparison of the results shows that the method in this paper achieves good agreement with the literature. In Section 6, the uncertainties of the measured dielectric parameters were analyzed. Section 7 draws conclusions.

2. Theory of the BOR-FEM based on BOR cavities

A rotating body resonant cavity, shown in Fig. 3, consists of a dielectric material inside cavity V, a perfect electric conductor (PEC) boundary S_1 and the actual non-magnetic conductor boundary S_2. V is obtained by rotating the meridional plane Ω along the z-axis, $\varepsilon_{\mathrm{rd}}(\rho,z)$ denotes the complex relative permittivity of the isotropic dielectric material, nonuniform in the ρz plane (meridional plane) but uniform in φ, ∂S_1 and ∂S_2 denote the meridians of S_1 and S_2, respectively, and σ denotes the conductor boundary conductivity.

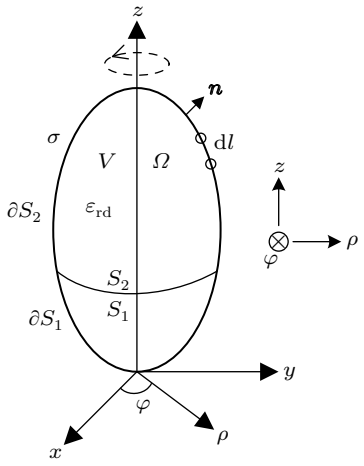


Fig. 3. The BOR resonant cavity.

Based on the above conditions, Maxwell's equations[36] are as follows:

$$\begin{aligned}
&\nabla\times\nabla\times\boldsymbol{E}-k_0^2\varepsilon_{\mathrm{rd}}\boldsymbol{E}=0,\\
&\boldsymbol{n}\times\boldsymbol{E}=0 \text{ on } S_1,\\
&\boldsymbol{n}\times(\nabla\times\boldsymbol{E})+\gamma_{\mathrm{e}}\boldsymbol{n}\times(\boldsymbol{n}\times\boldsymbol{E})=0 \text{ on } S_2,\\
&\gamma_{\mathrm{e}}=\mathrm{j}\frac{k_0}{\eta_{\mathrm{rc}}}=\mathrm{j}\frac{\omega\sqrt{\varepsilon_0\mu_0}}{\sqrt{1/(1-\mathrm{j}\sigma/\omega\varepsilon_0)}}\\
&\quad=\mathrm{j}\omega\sqrt{\mu_0\varepsilon_0-\mathrm{j}\sigma\mu_0/\omega},
\end{aligned}\tag{1}$$

where γ_{e} is the finite metal wall parameter, $\boldsymbol{n}$ is unit normal vector on ∂S_2, η_{rc} is the wave impedance on S_2 and k_0 is the vacuum propagation constant. Applying the Rayleigh–Ritz[36] principle to Eq. (1), the variational equation is

$$\begin{aligned}
F(\boldsymbol{E}) =\ &\frac{1}{2}\iiint_V\left[(\nabla\times\boldsymbol{E})\cdot(\nabla\times\boldsymbol{E})-k_0^2\varepsilon_{\mathrm{rd}}\boldsymbol{E}\cdot\boldsymbol{E}\right]\mathrm{d}V\\
&+\iint_{S_2}\left[\frac{\gamma_{\mathrm{e}}}{2}(\boldsymbol{n}\times\boldsymbol{E})\cdot(\boldsymbol{n}\times\boldsymbol{E})\right]\mathrm{d}S.
\end{aligned}\tag{2}$$

Based on the rotational symmetry of the resonant cavity, the electric field $\boldsymbol{E}$ in the resonant cavity is expanded as[37]

$$\boldsymbol{E}=\sum_{m=-\infty}^{\infty}\left(\boldsymbol{E}_{\mathrm{t}}^m(\rho,z)+\varphi E_\varphi^m(\rho,z)\right)\exp(\mathrm{j}m\varphi),\tag{3}$$

where the column coordinate system consists of the unit vectors $\boldsymbol{\rho}$, $\boldsymbol{\varphi}$, and $\boldsymbol{z}$, $\boldsymbol{E}_{\mathrm{t}}^m$ is the ρz plane component, E_φ^m is the φ

component and m is the order of the harmonic modes. There is no coupling between the different harmonic modes due to the orthogonality of the harmonic modes, so Eq. (2) can be expanded as a superposition of all the harmonic modes

$$\begin{aligned} F(\boldsymbol{E}) = \sum_{m=0}^{\infty} \pi \iint_{\Omega} \rho \Bigg[& \left(\nabla_{\mathrm{t}} \times \boldsymbol{E}_{\mathrm{t}}^{m}\right) \cdot \left(\nabla_{\mathrm{t}} \times \boldsymbol{E}_{\mathrm{t}}^{-m}\right) \\ & + \left(\nabla_{\mathrm{t}} E_{\varphi}^{m} - \frac{\mathrm{j}m}{\rho} \boldsymbol{E}_{\mathrm{t}}^{m} + \rho \rho^{-1} E_{\varphi}^{m}\right) \\ & \times \left(\nabla_{\mathrm{t}} E_{\varphi}^{-m} - \frac{-\mathrm{j}m}{\rho} \boldsymbol{E}_{\mathrm{t}}^{-m} + \rho \rho^{-1} E_{\varphi}^{-m}\right) \Bigg] \mathrm{d}\rho\, \mathrm{d}z \\ & + \sum_{m=0}^{\infty} \Bigg\{ - \pi \iint_{\Omega} k_0^2 \varepsilon_{\mathrm{rd}} \left(\boldsymbol{E}_{\mathrm{t}}^{m} \cdot \boldsymbol{E}_{\mathrm{t}}^{-m} + E_{\varphi}^{m} E_{\varphi}^{-m}\right) \rho\, \mathrm{d}\rho\, \mathrm{d}z \\ & + \pi \int_{\partial S_2} \gamma_{\mathrm{e}} \left[\left(\boldsymbol{n} \times \boldsymbol{E}_{\mathrm{t}}^{m}\right) \cdot \left(\boldsymbol{n} \times \boldsymbol{E}_{\mathrm{t}}^{-m}\right) + E_{\varphi}^{m} E_{\varphi}^{-m}\right] \rho\, \mathrm{d}l \Bigg\}, \end{aligned} \tag{4}$$

where

$$\begin{aligned} \nabla &= \nabla_{\mathrm{t}} + \boldsymbol{\varphi} \frac{1}{\rho} \frac{\partial}{\partial \varphi}, \\ \nabla_{\mathrm{t}} &= \boldsymbol{\rho} \frac{\partial}{\partial \rho} + \boldsymbol{z} \frac{\partial}{\partial z}. \end{aligned} \tag{5}$$

The TM0np mode is discussed in this paper because TM0np modes operate in the re-entrant resonant cavity. Then Eq. (4) can be simplified as

$$\begin{aligned} F(\boldsymbol{E}) = & \iint_{\Omega} \rho \left(\nabla_{\mathrm{t}} \times \boldsymbol{E}_{\mathrm{t}}\right) \cdot \left(\nabla_{\mathrm{t}} \times \boldsymbol{E}_{\mathrm{t}}\right) \mathrm{d}\rho\, \mathrm{d}z \\ & - k_0^2 \iint_{\Omega} \varepsilon_{\mathrm{rd}} \rho \boldsymbol{E}_{\mathrm{t}} \cdot \boldsymbol{E}_{\mathrm{t}} \mathrm{d}\rho\, \mathrm{d}z \\ & + \gamma_{\mathrm{e}} \int_{\partial S_2} \left(\boldsymbol{n} \times \boldsymbol{E}_{\mathrm{t}}\right) \cdot \left(\boldsymbol{n} \times \boldsymbol{E}_{\mathrm{t}}\right) \mathrm{d}l \end{aligned} \tag{6}$$

with $m = 0$, $E_{\varphi} = 0$ and the superscript m omitted.

Adopting the high-order interpolation vector basis functions[36,38,40] to meet the demand for highly accurate measurement of the dielectric parameters, Eq. (6) is represented by the matrix equation

$$\begin{aligned} F(\boldsymbol{E}) &= \boldsymbol{E}^{\mathrm{T}} \cdot \boldsymbol{K} \cdot \boldsymbol{E} - \omega^2 \varepsilon_0 \mu_0 \boldsymbol{E}^{\mathrm{T}} \cdot \boldsymbol{M} \cdot \boldsymbol{E} \\ &\quad + \mathrm{j}\omega \sqrt{\varepsilon_0 \mu_0 - \mathrm{j}\sigma \mu_0 / \omega}\, \boldsymbol{E}^{\mathrm{T}} \cdot \boldsymbol{T} \cdot \boldsymbol{E}, \\ \boldsymbol{E} &= (E_1, E_2, \ldots, E_n)^{\mathrm{T}}, \\ \omega &= 2\pi f (1 - \mathrm{j}/2Q), \end{aligned} \tag{7}$$

where $\boldsymbol{K}$, $\boldsymbol{T}$, and $\boldsymbol{M}$ are the $n \times n$ matrices assembled from elemental matrices,[36] ω is the complex resonant angular frequency of the resonance cavity, f and Q are, respectively, resonance frequency and quality factor, E_i are the coefficients of the electric field on the edges and n is the total number of edges.

The generalized eigenvalue equation

$$\left(\boldsymbol{K} + \mathrm{j}\omega \sqrt{\varepsilon_0 \mu_0 - \mathrm{j}\sigma \mu_0 / \omega}\, \boldsymbol{T}\right) \cdot \boldsymbol{E} = \omega^2 \varepsilon_0 \mu_0 \boldsymbol{M} \cdot \boldsymbol{E} \tag{8}$$

can be derived according the stationary principle[36]

$$\partial F(\boldsymbol{E}) / \partial E_i = 0, \quad (i = 1, \ldots, n). \tag{9}$$

In dielectric measurement applications, the resonance and dielectric parameters can be solved for each other according to Eq. (8). The specific solution procedure will be explained in detail in Section 3.

3. Resonant parameters and complex relative permittivity ε_{r} solution

The resonant parameters (resonant frequency and Q-factor) shift when the resonant cavity is loaded with dielectrics and the offsets of the resonant parameters are related to the complex dielectric constant ε_{r}. Therefore, of the two mentioned variables, the other can be solved when one is known according to Eq. (8). However, there are two problems.

(i) Equation (8) is not a standard generalized eigenvalue equation due to the ω on both sides of Eq. (8), hence the resonant parameters ω cannot be solved directly in the case of known ε_{r}.

(ii) When extracting ε_{r} with the measured resonant parameters ω, the authors of Refs. [2,3,35] constantly adjusted the parameters $\varepsilon_{\mathrm{r_sim}}$ of the simulator to match the simulated resonant parameters ω' to the measured resonant parameters ω, and they deemed the adjusted $\varepsilon_{\mathrm{r_sim}}$ to be ε_{r}. However, these procedures are very time-consuming when $\varepsilon_{\mathrm{r_sim}}$ is changed frequently.

To overcome the above problems, the forward method and the inversion method will be discussed in the following.

3.1. Solving resonant parameters with known ε_{r}

Assume that the BOR resonant cavity is divided into m BOR regions filled with homogeneous dielectrics, as in Fig. 4, equation (8) is specified as

$$\begin{aligned} & \left(\boldsymbol{K} + \mathrm{j}\omega \sqrt{\varepsilon_0 \mu_0 - \mathrm{j}\sigma \mu_0 / \omega}\, \boldsymbol{T}\right) \cdot \boldsymbol{E} = \omega^2 \varepsilon_0 \mu_0 \boldsymbol{M} \cdot \boldsymbol{E}, \\ & \boldsymbol{M} = \sum_{i=1}^{m} \varepsilon_{\mathrm{rd},i} \boldsymbol{M}_i, \end{aligned} \tag{10}$$

where the known $\boldsymbol{M}_i$ is assembled from elemental matrices in the area Ω_i[36] and ω is the resonant parameter to be solved. Equation (10) can be solved by the iterative method, therefore adopting

$$\left(\boldsymbol{K} + \mathrm{j}\omega_k \sqrt{\varepsilon_0 \mu_0 - \mathrm{j}\sigma \mu_0 / \omega_k}\, \boldsymbol{T}\right) \cdot \boldsymbol{E} = \omega_{k+1}^2 \varepsilon_0 \mu_0 \boldsymbol{M} \cdot \boldsymbol{E}. \tag{11}$$

First, assuming that ω_k has been solved, ω_{k+1} is solved by the methods of Refs. [41,42]. Second, ω_k is replaced with ω_{k+1}.

Finally, ω_k converges to the solution ω of Eq. (8) by repeating the above process. The iterative process of Eq. (11) is shown in Fig. 5. The experimental results show that ω_k converges to the solution ω of Eq. (8) if the initial value ω_1 is chosen to be near ω.

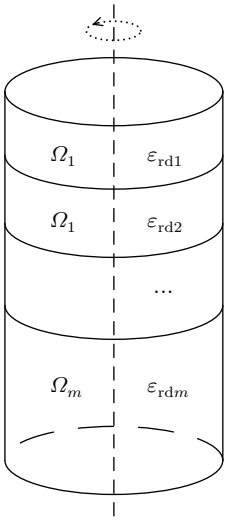


Fig. 4. BOR resonant cavity divided into m BOR regions filled with homogeneous dielectrics.

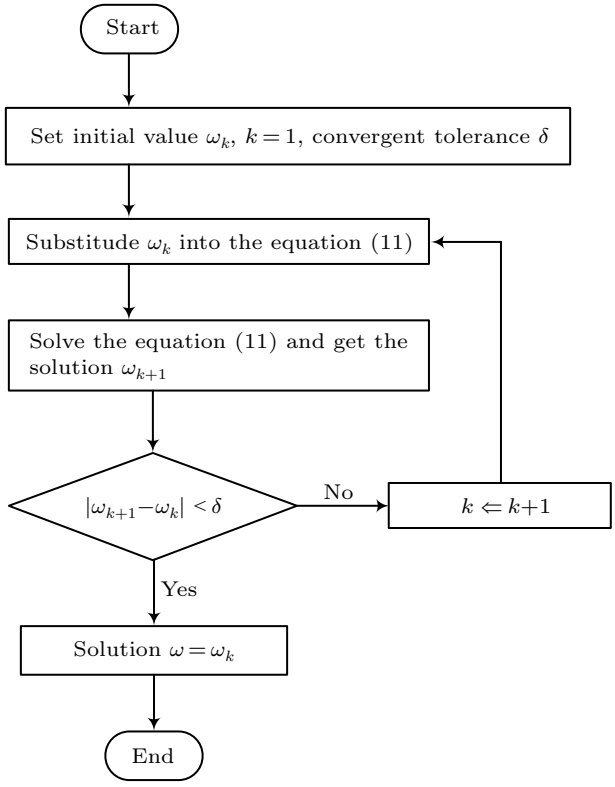


Fig. 5. The iterative procedure for solving Eq. (8).

3.2. Solving ε_r with measured resonant parameters

In dielectric measurement applications, the resonant cavity is divided into the sample region (Ω_1) and the air region (Ω_2); therefore the matrix $\boldsymbol{M}$ is

$$\boldsymbol{M} = \varepsilon_r \boldsymbol{M}_1 + \boldsymbol{M}_2. \tag{12}$$

This is substituted into Eq. (8) to get the following equation:

$$\left(\boldsymbol{K} + \mathrm{j}\omega\sqrt{\varepsilon_0\mu_0 - \mathrm{j}\sigma\mu_0/\omega}\boldsymbol{T} - \omega^2\varepsilon_0\mu_0\boldsymbol{M}_2\right)\cdot\boldsymbol{E} = \omega^2\varepsilon_0\mu_0\varepsilon_r\boldsymbol{M}_1\cdot\boldsymbol{E}. \tag{13}$$

From Eq. (13), ε_r can be solved directly using the methods of Refs. [41,42] with the measured ω, avoiding tedious work to determine dielectric parameters by continuously adjusting the dielectric parameters to match the computing frequencies to the measured frequencies.

4. Verification and comparison

In order to demonstrate the accuracy and efficiency of the proposed method, there is a comparison between the proposed method, the literature and the HFSS with the PC configuration Intel Core i5-9600k and 16 GB RAM.

4.1. Cylindrical cavity coaxially loaded with two dielectric materials

In Fig. 6(a), assume that the electric conductor wall of the cylindrical resonant cavity, coaxially loaded with two dielectric materials that fill it along the cavity height, is a PEC as in Ref. [24].

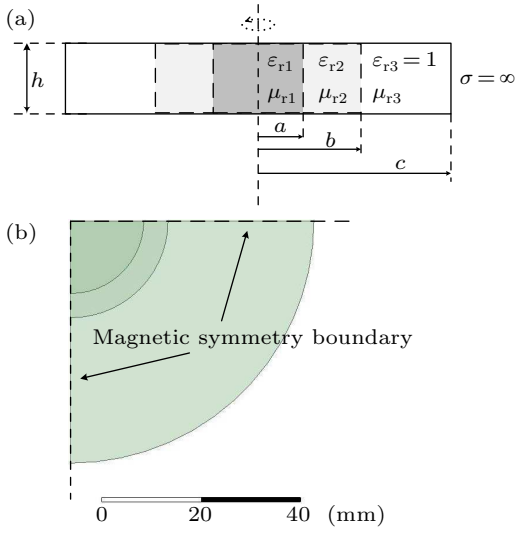


Fig. 6. The cylindrical cavity coaxially loaded with dielectric materials. (a) Sectional view of the structure. (b) Two magnetic symmetry boundaries set in the HFSS.

The results obtained by Penaranda-Foix *et al.*[24] using the new four-port ring network based on the MM method are consistent with the analytical solutions. Therefore, it is meaningful to compare the BOR-FEM results with those in Ref. [24] and those using other methods. In order to reduce the HFSS simulation time, two magnetic symmetry boundaries of the HFSS simulation process are adopted in Fig. 6(b) due to the rotational symmetry of the TM0*np* modes.

Table 1 compares the computed resonance parameters of the TM0*np* (TM010 and TM020) modes obtained by BOR-FEM, Penaranda-Foix *et al.*[24] and the HFSS simulation. The

size of the cylindrical resonant cavity and the dielectric parameters are also given.

Table 2 compares the calculating performance between the BOR-TEM method and the HFSS. From Table 2, the results obtained with the BOR-FEM are almost equal to those in Ref. [24] and the HFSS. Furthermore, Table 2 shows that the computation time and the number of elements of BOR-FEM are much smaller than those of the HFSS, showing the high accuracy and high efficiency of the BOR-FEM method.

Table 1. Resonant frequency comparisons $a = 15$ mm, $b = 20$ mm, $c = 50$ mm, $h = 20$ mm.

Mode	Method	f (MHz)	Q
TM010	analytical and Ref. [24]	1873.6	144.536
$\varepsilon_{r1} = 2(1 - j \times 10^{-2})$	this paper	1873.6	144.536
$\varepsilon_{r2} = 2(1 - j \times 10^{-2})$	HFSS	1873.7	144.537
TM020	analytical and Ref. [24]	4578.8	265.069
$\varepsilon_{r1} = 2(1 - j \times 10^{-2})$	this paper	4578.8	265.068
$\varepsilon_{r2} = 2(1 - j \times 10^{-2})$	HFSS	4578.9	265.069
TM010	analytical and Ref. [24]	1302.0	11444.3
$\varepsilon_{r1} = 5(1 - j \times 10^{-4})$	this paper	1302.0	11444.3
$\varepsilon_{r2} = 5(1 - j \times 10^{-4})$	HFSS	1302.7	11444.3
TM020	analytical and Ref.[24]	3735.6	16965.3
$\varepsilon_{r1} = 5(1 - j \times 10^{-4})$	this paper	3735.6	16965.3
$\varepsilon_{r2} = 5(1 - j \times 10^{-4})$	HFSS	3737.6	16965.1
TM010	analytical and Ref. [24]	1432.2	698.79
$\varepsilon_{r1} = 5(1 - j \times 10^{-4})$	this paper	1432.2	698.79
$\varepsilon_{r2} = 2(1 - j \times 10^{-2})$	HFSS	1432.9	698.79

Table 2. Calculated performance comparisons.

Method	Number of elements	Computing time (s) per solution
BOR-FEM	99	0.2
HFSS (FEM)	99258	420

4.2. Cylindrical cavity partially and coaxially loaded with a dielectric disk

A cylindrical cavity partially and coaxially filled with a dielectric disc, as shown in Fig. 7, is assumed to be a PEC, as in Ref. [24]. The size and dielectric parameters are given in Table 3 and are the same in Refs. [24,43] (Ref. [43] applied the orthonormal-basis method). The results show that the resonant frequencies computed in this paper agree better with those in Ref. [24] than those in Ref. [43], verifying again the high-accuracy and high efficiency of the BOR-FEM.

Table 3. Resonant frequency (MHz) comparisons ($\varepsilon_{r1} = 35.74$, $a = 8.636$ mm, $b = 12.95$ mm, $h_1 = h_3 = 3.81$ mm, $h_2 = 7.62$ mm).

Mode	Ref. [43]	Ref. [24]	This paper	Relative error (%) compared with Refs. [24,43] respectively
TM01	4568	4541.0	4540.832	0.5983, 0.0037
TM02	6384	6373.2	6372.548	0.1797, 0.0102
TM03	7323	7262.2	7262.247	0.8365, −0.0006
TM04	7685	7661.4	7661.236	0.3101, 0.0021
TM05	9169	9107.8	9107.781	0.6721, 0.0002
TM06	10031	9982.7	9982.697	0.48380, 0.00003

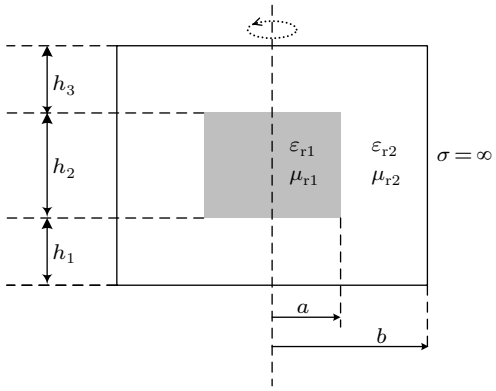


Fig. 7. Cylindrical cavity partially equipped with a dielectric disc.

4.3. Re-entrant cavity with an insertion hole

A re-entrant cavity with an insertion hole is shown in Fig. 2, and its dimensions (shown in Fig. 8) are given in Table 4, where $2r_s$ is the diameter of the sample cylinder and $2r_1$ is the diameter of the insertion hole.

Table 4. The size of the re-entrant cavity (mm).

r_{out}	r_{in}	$2r_1$	d_1	d_2	d_3	h_{out}	h_{in}
32.00	9.15	6.05	15.45	18.00	2.50	190.00	186.50

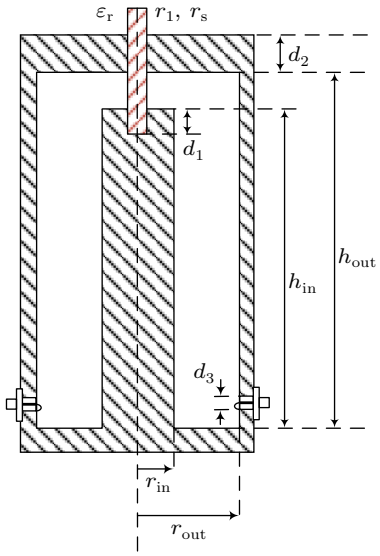


Fig. 8. The dimensions of the re-entrant resonant cavity.

This experiment adopted two loop couplings, and details of these are described in Section 5. The simulation procedure excludes the loop couplings to guarantee the geometric rotational symmetry of the re-entrant cavity. During the experiment, the re-entrant cavity is working in the TM01p modes ($p = 1, 2, 3, 4, 5$).

The results of the resonant parameters computed in this work, by the HFSS and with Comsol are given in Table 5, assuming the conductivity is 5.8×10^7 S·m^{-1} (copper) selected from HFSS. The comparison shows that the relative error of the resonant frequency is 9×10^{-3}% and the relative error of the Q-factor is 0.3%.

Table 5. The results for the resonant parameters computed by this paper, the HFSS and Comsol.

Mode	Method	f (MHz)	Q
TM011	this paper	349.606	4645.80
	HFSS	349.576	4635.57
	Comsol	349.608	4644.70
TM012	this paper	1056.976	7971.22
	HFSS	1056.942	7951.39
	Comsol	1056.974	7970.12
TM013	this paper	1781.979	10178.59
	HFSS	1782.033	10150.26
	Comsol	1781.971	10176.50
TM014	this paper	2523.976	11945.62
	HFSS	2524.162	11913.81
	Comsol	2523.980	11942.23
TM015	this paper	3278.435	13469.85
	HFSS	3278.672	13430.12
	Comsol	3278.440	13468.88

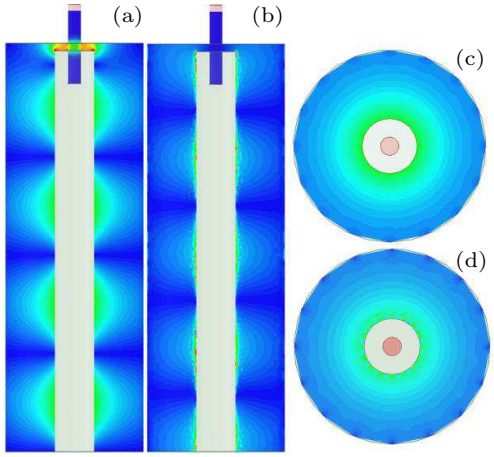


Fig. 9. (a) Electric and (b) magnetic fields on the meridional plane. (c) Electric and (d) magnetic fields on the intersecting surface.

The amplitude of the electric and magnetic fields is plotted in Fig. 9. According to Figs. 9(a) and 9(b), the assumption that the insertion holes are below the cutoff frequency are proved, because the electric and magnetic fields vanish at the insertion holes. That is, the resonant parameters are independent of the depth of the bottom insertion hole (d_1) and the height of the top insertion hole (d_2). In Figs. 9(c) and 9(d), the electric and magnetic fields are symmetric about the rotation axis.

5. Measurement results and discussion

The experimental setup, shown in Fig. 10, consists of a vector network analyzer (VNA; Keysight Technologies, N5227B PNA), two high-stability VNA cables and a re-entrant resonant cavity that is machined from brass with gold plating and has the same dimensions as in Fig. 8. The loop couplings are near the end walls of the coaxial line (Fig. 2) and $d_3 = 2.5$ mm (Table 4). They were adjusted to ensure weak coupling ($S_{21} < -35$ dB), therefore the deviation of the measured resonant parameters is negligible. Although the cavity with the loop couplings is not rotationally symmetric, the BOR-FEM is still effective under the condition of weak coupling.

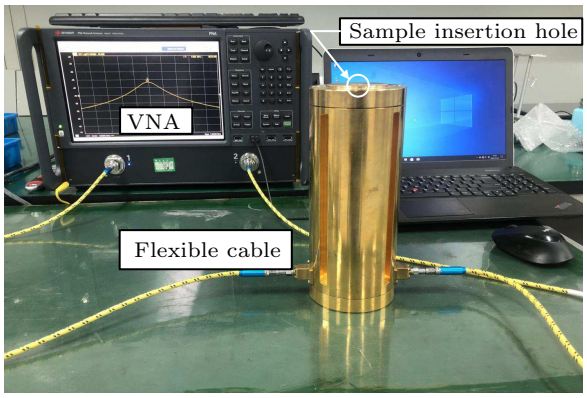


Fig. 10. The test system for the re-entrant resonance cavity.

The experiments were performed at room temperature (about 22 °C), therefore, interference from temperature was negligible. The intermediate-frequency bandwidth was set to 1 kHz and the VNA cables were connected to perform the corresponding calibration. According to Table 5, the resonant frequency of the TM011 mode is about 350 MHz and the resonant frequency of the TM015 mode is about 3.2 GHz. In order to accurately measure those mode parameters, the frequency sweep was set from 0.2 GHz to 3.5 GHz to cover those mode frequencies, and the resonant parameters were determined by the S_{21} parameter.

During the experiment, the center axis of the sample deviates a little from that of the cavity, causing deviations in the measured resonant parameters, because the sample cylinder diameter ($2r_s$) is a little smaller than the insertion hole diameter ($2r_1$). Another condition is that the sample is an imperfect cylinder due to errors in machining technology. However, the BOR-FEM remains effective under these situations. In order to modify the concentricity of the cylindric sample and insertion holes, the limiter, shown in Fig. 11, was used to allow the sample to be inserted through the central axis of the cavity. The limiter has little effect on the measurement because the insertion holes below the cutoff frequency were certified as in Subsection 4.3.

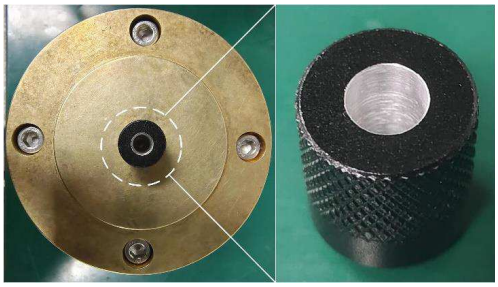


Fig. 11. The combination of limiter and re-entrant cavity.

Although the sample is inserted through the center axis of the cavity, the measured dielectric parameters are sensitive to $2r_s$. This factor ($2r_s$) will be analyzed as an uncertainty variable in Section 6.

Referring to Subsection 4.3, the insertion holes of the cavity are below the cutoff frequency for eliminating the radiated field. To analyze this condition, the insertion holes are assumed to be circular waveguides. Since TE11 is the fundamental mode, the resonant frequency below the cutoff frequency of the TE11 mode can dramatically lower the radiation from the holes. The cutoff frequency f_{TE11} of the TE11 mode is

$$f_{\mathrm{TE11}} = \frac{1.8412 c_0}{2\pi r_1 \sqrt{\varepsilon_{\mathrm{r}}}}, \tag{14}$$

where r_1, ε_{r}, and c_0 are the radius of the insertion hole, the permittivity of the sample and the velocity of light in a vacuum, respectively. The relationship between the f_{TE11} and ε_{r} is shown in Table 6.

Therefore, the first five modes listed in Table 5 are easily below f_{TE11} at $\varepsilon_{\mathrm{r}} = 20$. For dielectrometry applications, the sensitivities of the resonant frequency of those modes are shown in Fig. 12 as a function of ε_{r}. The greater the variation in the resonant frequency of a certain mode, the more sensitive that mode is, therefore, the higher the accuracy with which ε_{r} can be extracted.

The first five resonance parameters of the resonant cavity were measured and are shown in Table 7, where f and Q are the resonant frequency and Q-factor, respectively, and the uncertainties of $u(f)$ and $u(Q)$ were computed by repeating the measurements 10 times. The dielectric parameters of the three samples (PTFE, fused silica and Al_2O_3) were computed by the BOR-FEM and are compared with the results from Refs. [23,44,45] (Table 8). Compared with the reference data, the relative differences for PTFE, fused silica and Al_2O_3 are less than 1.1% and 12.8% in the real and imaginary parts of the complex permittivities, respectively. The calculation time of each dielectric parameter is 0.8 s, which again verifies the high accuracy and efficiency of the proposed method.

Table 6. The relationship between f_{TE11} and ε_{r} ($r_1 = 3.025$ mm, $c_0 = 3 \times 10^{11}$ mm·s^{-1}).

ε_{r}	f_{TE11} (MHz)
1	29 061
5	12 997
10	9190
15	7504
20	6498

Table 7. The results of the resonant parameter measurements.

Material	Mode	f (MHz)	$u(f)$ (MHz)	Q	$u(Q)$
Unloaded	TM011	348.659	0.002	4461.5	15.6
	TM012	1054.792	0.005	7104.1	21.3
	TM013	1779.429	0.010	8512.3	12.6
	TM014	2521.335	0.006	9432.2	17.2
	TM015	3275.773	0.001	9930.2	19.3
PTFE	TM011	346.865	0.001	4315.4	12.4
	TM012	1050.476	0.003	6802.2	16.5
	TM013	1774.161	0.005	8200.1	14.9
	TM014	2516.115	0.005	9141.6	13.4
	TM015	3270.986	0.004	9697.7	15.2
Fused silica	TM011	344.172	0.020	4333.8	11.3
	TM012	1043.925	0.020	6851.6	19.4
	TM013	1766.266	0.025	8239.7	18.4
	TM014	2508.340	0.020	9186.0	17.6
	TM015	3263.799	0.030	9718.0	13.1
Al_2O_3	TM011	340.668	0.040	4187.1	13.6
	TM012	1035.477	0.050	6553.3	12.7
	TM013	1756.249	0.050	7891.0	14.5
	TM014	2498.392	0.060	8923.7	11.7
	TM015	3254.472	0.070	9476.3	11.1

Table 8. Comparison between the results from the BOR-FEM and the literature for dielectric parameter measurement.

Material	$2r_s$ (mm)	Mode	This work				Other measurements		
			ε'	$u(\varepsilon')$ (10^{-2})	ε'' (10^{-4})	$u(\varepsilon'')$ (10^{-4})	ε'	ε'' (10^{-4})	Ref.
PTFE	5.95	TM011	2.067	1.89	7.4	1.10	2.066	7.0	[44]
		TM012	2.042	1.81	7.6	0.74			
		TM013	2.045	1.84	7.4	0.54			
		TM014	2.047	1.88	7.9	0.68			
		TM015	2.048	1.92	7.8	0.96			
Fused silica	5.92	TM011	3.868	6.47	6.2	1.19	3.850	5.5	[23]
		TM012	3.843	6.20	6.0	0.90			
		TM013	3.854	6.28	5.9	0.70			
		TM014	3.858	6.38	5.8	0.89			
		TM015	3.865	6.49	5.9	1.05			
Al_2O_3	5.52	TM011	9.042	17.8	26.5	2.54	9.078	27	[45]
		TM012	9.036	17.3	27.2	1.64			
		TM013	9.059	17.7	29.2	1.42			
		TM014	9.098	18.5	24.8	1.57			
		TM015	9.091	18.8	25.9	1.96			

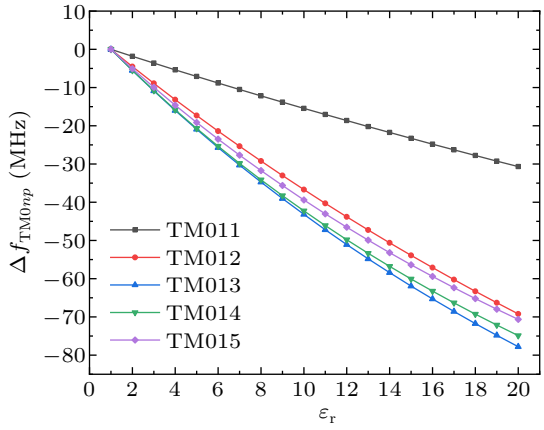


Fig. 12. Variation of the shift of the resonant frequency as a function of ε_{r}.

6. Uncertainty analysis

The standard uncertainty equation for evaluating the uncertainties of the measured dielectric parameters[46] is

$$u^2(y) = \sum_{i=1}^{N} \left(\frac{\partial \varepsilon}{\partial x_i} \right)^2 u^2(x_i), \tag{15}$$

where ε is the dielectric parameter and x_i is the independent variable that ε depends on. The term $u(x_i)$ is the uncertainty of each independent variable and the partial derivative $(\partial\varepsilon/\partial x_i)$ is the sensitivity coefficient.

The main independent variables include the sizes of the re-entrant cavity, the gap between the sample cylinder ($2r_{\mathrm{s}}$) and the insertion holes ($2r_1$), environmental temperature, coupling network, probe positioning and the resonant parameters derived from the VNA measurements.

The depth of the bottom insertion hole (d_1) and the height of the top insertion hole (d_2) will not be taken into account in the uncertainty analysis since they have been verified in Subsection 4.3. The uncertainty of the environmental temperature (22 °C), the interference of the coupling network and probe positioning are negligible as discussed in Section 5.

Although the VNA adopted high-precision settings, there are still errors in resonance parameters measured from the VNA, especially the Q-factor. The uncertainties of the unloaded resonant parameters (f_{u} and Q_{u}) and the loaded resonant parameters (f_{L} and Q_{L}) were given in Table 7. In addition, due to errors in machining technology of the resonant cavity and sample, dimensional uncertainty variants are listed in Table 9 according to current machining technology. The partial derivative terms of Eq. (15) were computed by numerical methods because of the difficulty of calculating these by analytical methods.

The uncertainty of the PTFE (TM013) is calculated with this procedure, and is shown in Table 9. From Table 9, the manufacturing tolerances of the sample cylinder ($2r_{\mathrm{s}}$) have the highest influence on the total uncertainty in ε'. This is because the electric field is concentrated near the insertion holes, therefore it is meaningful to improve the machining precision of the sample cylinder. The uncertainties in the measured Q-factor (Q_{u} and Q_{L}) also have a large influence on ε''. For all samples and resonant modes, the uncertainty was within the range of 2.06% for ε' and 20% for ε''.

Table 9. Uncertainty contributions to the total uncertainty for PTFE TM013.

x_i	$u(x_i)$	$\frac{\partial\varepsilon'}{\partial x_i}u(x_i)$	$\frac{\partial\varepsilon''}{\partial x_i}u(x_i)$
r_{out}	0.02 mm	3.27×10^{-4}	2.3×10^{-7}
z_{out}	0.02 mm	1.59×10^{-3}	1.1×10^{-6}
r_{in}	0.02 mm	3.22×10^{-3}	2.2×10^{-6}
z_{in}	0.02 mm	1.73×10^{-3}	1.2×10^{-6}
$2r_1$	0.02 mm	9.01×10^{-3}	8.2×10^{-6}
$2r_{\mathrm{s}}$	0.02 mm	1.53×10^{-2}	1.3×10^{-5}
f_{u}	0.010 MHz	2.07×10^{-3}	8.6×10^{-8}
Q_{u}	12.6	0.00	3.2×10^{-5}
f_{L}	0.005 MHz	1.03×10^{-3}	4.3×10^{-8}
Q_{L}	14.9	0.00	4.0×10^{-5}
$u(\varepsilon)$		1.84×10^{-2}	5.4×10^{-5}

7. Conclusion

The BOR-FEM can transform 3D problems into 2D problems for structures that are symmetrical about the rotation axis, greatly reducing the matrix size; this not only ensures high precision of the FEM but also greatly improves the solution speed. The BOR-FEM was applied to representative structures and was compared with other methods, showing high accuracy and fast computing speed. This proposed method was also applied to measure dielectric parameters using the re-entrant cavities with insertion holes. The measurement results showed good agreement with the literature (1.1% and 12.8% relative differences in the real and imaginary parts of the complex permittivities, respectively). Finally, according to the uncertainty analysis in this paper, it is known that the uncertainties in the sample diameter and measured Q-value have a large impact on the measurement results for ε' and ε''.

The BOR-FEM is suitable for measurements of the permittivity of isotropic materials. Because Eq. (1) only considers isotropic dielectric materials, if magnetic materials are to be considered the permeability parameters should be added to Eq. (1). However, the BOR-FEM has not been applied to the measurement of anisotropic materials at present, although the structures of samples and the resonant cavity have geometric rotational symmetry; this will be considered in future work.

Acknowledgments

Project supported by the National Natural Science Foundation of China (Grant No. 62001083) and the Guangdong Provincial Key Research and Development Project, China (Grant No. 2020B010179002).

References

[1] Holzman E L 2006 *IEEE Trans. Microw. Theory* **54** 3127
[2] Deshpande M D, Reddy C J, Tiemsin P I, *et al.* 1997 *IEEE Trans. Microw. Theory* **45** 359
[3] Santra M and Limaye K U 2005 *IEEE Trans. Microw. Theory* **53** 718
[4] Baker-Jarvis J, Janezic M D and DeGroot D C 2010 *IEEE Instrum. Meas. Mag.* **13** 24
[5] Kaatze U and Hubner C 2010 *Meas. Sci. Technol.* **21** 082001
[6] Kaatze U 2010 *Metrologia* **47** S91
[7] Krupka J 2006 *Meas. Sci. Technol.* **17** R55
[8] Le Floch J M, Fan Y, Humbert G, *et al.* 2014 *Rev. Sci. Instrum.* **85** 031301
[9] Janezic M D and Baker-Jarvis J 1999 *IEEE Trans. Microw. Theory* **47** 2014
[10] Janezic M D and Grosvenor J H 1991 *Conference Record. IEEE Instrumentation and Measurement Technology Conference*, May 14–16, 1991, p. 580
[11] Geyer R G, Kabos P and Baker-Jarvis J 2002 *IEEE Trans. Instrum. Meas.* **51** 383
[12] Costa F, Monorchio A, Amabile C, *et al.* 2011 2011 41*st European Microwave Conference*, October 10–13, 2011, p. 945
[13] Xiang Y H, Huang J, Fu L L, *et al.* 2021 *IEEE Sens. J.* **21** 10657
[14] Penaranda-Foix F L, Catala-Civera J M, Canos-Marin A J, *et al.* 2009 *2009 IEEE MTT-S International Microwave Symposium Digest*, June 7-12, 2009, p. 1309
[15] Zhou Y, Li E, Guo G F, *et al.* 2011 *Aerospace Materials & Technology* **41** 60 (in Chinese)
[16] Guo Y F, Zhang Z C and Fu C J 2011 *High Power Laser and Particle Beams* **23** 731
[17] Marques-Villarroya D, Penaranda-Foix F, Garcia-Banos B, *et al.* 2017 2017 47*th European Microwave Conference (EuMC)*, October 10–12, 2017, p. 440
[18] Fan Y H, Zhang Z Y, Carvalho N C, *et al.* 2014 *IEEE Trans. Microw. Theory* **62** 1657
[19] Barroso J J, Castro P J, Neto J P L, *et al.* 2005 *SBMO/IEEE MTT-S International Conference on Microwave and Optoelectronics,* 2005. July 25, 2005, p. 129
[20] Xi W G and Tinga W R 1992 *IEEE Trans. Microw. Theory* **40** 1927
[21] Wexler A 1967 *IEEE Trans. Microw. Theory* **15** 508
[22] Khodja A, Tounsi M L and Lamhene Y 2002 2002 3*rd International Conference on Microwave and Millimeter Wave Technology,* 2002. *Proceedings. ICMMT* 2002. August 17–19, 2002, p. 630
[23] Marques-Villarroya D, Penaranda-Foix F L, Garcia-Banos B, *et al.* 2017 *IEEE Trans. Microw. Theory* **65** 1191
[24] Penaranda-Foix F L, Janezic M D, Catala-Civera J M, *et al.* 2012 *IEEE Trans. Microw. Theory* **60** 2730
[25] Lech R and Mazur L 2007 *IEEE Trans. Microw. Theory* **55** 2115
[26] Thompson F, Haigh A D, Dillon B M, *et al.* 2003 *IEE Proc. - Sci. Meas. Technol.* **150** 113
[27] Kanai Y, Tsukamoto T, Miyakawa M, *et al.* 2000 *IEEE Trans. Magn.* **36** 1750
[28] Hano M 1984 *IEEE Trans. Microw. Theory* **32** 1275
[29] Zhang C F, Wang W, An S G, *et al.* 2021 *Chin. Phys. B* **30** 010101
[30] Castiblanco J A, Seetharamdoo D, Berbineau M, *et al.* 2015 *IEEE Trans. Antenn. Propag.* **63** 1086
[31] Jia P H, Liu Q H, Chen Y P, *et al.* 2020 *IEEE Trans. Antenn. Propag.* **68** 4753
[32] Dunn E A, Byun J K, Branch E D, *et al.* 2006 *IEEE Trans. Antenn. Propag.* **54** 945
[33] Zhou Q, Lin S P, Zhang P, *et al.* 2019 *Acta Phys. Sin.* **68** 147104 (in Chinese)
[34] Zhu Z H, Chen M S, Wu X L, *et al.* 2014 *Computer Technology and Development* **24** 51 (in Chinese)
[35] Mumcu G, Sertel K and Volakis J L 2008 *IEEE Trans. Microw. Theory* **56** 217
[36] Jin J M 2002 *The Finite Element Method in Electromagnetics,* 2*nd Edition* (New York: John Wiley & Sons) p. 193
[37] Greenwood A D and Jin J M 1999 *IEEE Trans. Antenn. Propag.* **47** 620
[38] Graglia R D, Wilton D R and Peterson A F 1997 *IEEE Trans. Antenn. Propag.* **45** 329
[39] Kameari A 1990 *IEEE Trans. Magn.* **26** 466
[40] Webb J P and Forgahani B 1993 *IEEE Trans. Magn.* **29** 1495
[41] Stewart G W 2002 *SIAM J. Matrix Analysis Appl.* **23** 601
[42] Stewart G W 2000 *Math Comput.* **69** 1309
[43] Monsoriu J A, Andres M V, Silvestre E, *et al.* 2002 *IEEE Trans. Microw. Theory* **50** 2545
[44] Catala-Civera J M, Canós A J, Plaza-González P, *et al.* 2015 *IEEE Trans. Microw. Theory* **63** 2905
[45] Yu C Y, Tu Y H, Zhang Y P, *et al.* 2021 *IEEE Access* **9** 14807
[46] Gutiérrez-Cano J D, Plaza-González P, Canós A J, *et al.* 2020 *IEEE Trans. Instrum. Meas.* **69** 3595